POLITECNICO DI TORINO
Repository ISTITUZIONALE

Automatic Localized Nonconformal Mesh Refinement for Surface Integral Equations

Original
Automatic Localized Nonconformal Mesh Refinement for Surface Integral Equations / Tobon Vasquez, Jorge A.; Peng, Zhen; Lee, Jin-Fa; Vecchi, Giuseppe; Vipiana, Francesca. - In: IEEE TRANSACTIONS ON ANTENNAS AND PROPAGATION. - ISSN 0018-926X. - STAMPA. - 68:2(2020), pp. 967-975. [10.1109/TAP.2019.2944551]

Availability:
This version is available at: 11583/2789097 since: 2020-02-05T10:14:15Z

Publisher:
IEEE Antennas and Propagation Society

Published
DOI:10.1109/TAP.2019.2944551

Terms of use:

This article is made available under terms and conditions as specified in the corresponding bibliographic description in the repository

Publisher copyright
IEEE postprint/Author's Accepted Manuscript

©2020 IEEE. Personal use of this material is permitted. Permission from IEEE must be obtained for all other uses, in any current or future media, including reprinting/republishing this material for advertising or promotional purposes, creating new collecting works, for resale or lists, or reuse of any copyrighted component of this work in other works.

(Article begins on next page)

24 April 2024

Automatic Localized Non-Conformal Mesh Refinement for Surface Integral Equations

J. A. Tobon Vasquez, *Member, IEEE*, Z. Peng, *Member, IEEE*, J. F. Lee, *Fellow, IEEE*, G. Vecchi, *Fellow, IEEE* and F. Vipiana, *Senior Member, IEEE*

***Abstract*—We propose an automatic, solution based, localized meshing refinement for increasing the accuracy of integral-equation solution for multi-scale electromagnetic problems. The procedure starts with a local measure of the boundary condition error, via testing on zero-order basis functions defined on the finest level mesh. Then, the adaptive mesh refinement (h-refinement) is obtained by non-conformal sub-meshing with Discontinuous Galerkin formulation in order to achieve the desired accuracy. Numerical experiments shows the effectiveness of the approach in the cases of cubic geometry and realistic multi-scale structures.**

***Index Terms*—Integral equations, method of moments, adaptive mesh refinement, discontinuous Galerkin, error estimation.**

I. Introduction

Mesh quality and resolution are key issues in the accurate and efficient solution to many numerical problems. If the numerical method is well tested and well conditioned, even in multi-scale problems, the solution accuracy is proportional to mesh density. However, there is an obvious need to trade off between mesh density and computational cost. One challenge is how to achieve a desired level of accuracy for both smooth parts and non-smooth parts (geometrical asperities, edges, corners, etc.) of the object. In general, the adaptive refinement consists of two necessary parts: detection of inaccuracies, and schemes to increase accuracy by locally acting in targeted regions.

The study of adaptive refinement procedures has prompted a large body of research in finite elements, e.g. [1]–[4]. For surface integral equation methods, local a-posteriori error estimation techniques have been proposed to identify high-error regions in the case of 2-D simple geometries, e.g. [5]–[9]. In [10], a simple error metric, based on checking boundary conditions on the scatterer surface, is applied to 3-D geometries to identify the contributions of the mesh cells to the total error. Moreover, in [11]–[13] Ubeda and co-authors presented a geometrically based mesh refinement procedure devoted to improve the solution accuracy in presence of sharp edges. Finally, in [14], an adaptive h-refinement based on an advancing front Delaunay triangulation and Laplacian smoothing has been proposed for the numerical solution of the electric field integral equation (EFIE).

In this work, we propose an automatic refinement for the surface integral equation analysis of complex 3-D bodies. The goal of this study is to adaptively choose the resolution of approximation for a desired level of accuracy in the analysis of multi-scale structures. Due to the Calderon identity [15], the error in the approximate solution can be bounded above and below by the residual error of the discretized surface integral equation. This means that locally refining the mesh where the residual is larger actually improves the overall accuracy. We therefore develop an a-posteriori error estimator based on the residual error associated with individual elements, where an automatic localized meshing refinement, based on dyadic subdivisions, is applied to the elements above a predefined error threshold. The proposed scheme does not fully respect all the hypothesis in [15], implementing also not div-conforming basis functions and considering geometries with non-smooth parts; however, the obtained numerical results are in line the ones theoretically predicted in [15].

In order to achieve meshing efficiency, this paper exploits a very appealing feature of the recently developed discontinuous Galerkin boundary element method [16], [17]. For a given discretization, the resolution of approximation can be adapted at the element level to align with the operating frequency and local characteristics of the problem geometry. It is directly applicable to multi-scale problems, which feature electrically small, geometrically complex regions, and regions that are smooth and electrically large.

The paper is organized as follows. In Sect. II surface integral equations and discontinuous Galerkin (DG) are briefly reviewed to set the notation. In Sect. III the proposed automatic refinement scheme is discussed in details. Numerical examples are in Sect. IV and finally Sect.V contains the conclusions and future perspectives. Preliminary results have been presented in [18]–[21].

II. Background: Surface Integral Equation and Discontinuous Galerkin

The linear system, corresponding to the Combined Field Integral Equation (CFIE) used to analyze a perfect electric conductor (PEC) close body in free space, can be written as:

$$\left(\frac{[Z_{\mathrm{EFIE}}]}{\eta}+\alpha[Z_{\mathrm{MFIE}}]\right)[I]=\frac{[V_{\mathrm{EFIE}}]}{\eta}+\alpha[V_{\mathrm{MFIE}}] \quad (1)$$

where η is the intrinsic impedance, used to normalize the matrices in order to have similar dimensions and magnitudes, and α is a dimensionless weight, controlling the contribution of the Electric Field Integral Equation (EFIE) and Magnetic Field Integral Equation (MFIE) operators. The matrices $[Z_\beta]$ and the vectors $[V_\beta]$, with $\beta = \mathrm{EFIE}$ or MFIE, represent the MoM matrices and right hand side (RHS) vectors corresponding to the EFIE and MFIE formulations. Finally the vector $[I]$ collects the coefficients of the basis functions $\mathbf{f}_n$ chosen to

discretize the unknown electric surface current density $\mathbf{J}$, e.g. the RWG basis functions [22],

$$\mathbf{J}(\mathbf{r}) \simeq \sum_{n=1}^{N} I_n \mathbf{f}_n(\mathbf{r}), \tag{2}$$

where N is the total number of basis functions and $\mathbf{r}$ is a generic point on the body surface. The $[Z_{\mathrm{EFIE}}]$ can be written as

$$[Z_{\mathrm{EFIE}}] = [Z^{\phi}] + [Z^{A}] \tag{3}$$

where the contributions of the scalar (ϕ) and vector (A) potentials are explicitly denoted.

When non div-conforming basis function $\mathbf{f}_n$ are used for the DG approach, there is a significant change in the evaluation of $[Z^{\phi}]$. A generic basis function $\mathbf{f}_n$, non-zero only inside a discretization cell, can be always written as

$$\mathbf{f}_n(\mathbf{r}) = \mathbf{f}_n^C(\mathbf{r})\chi(\mathbf{r}) \tag{4}$$

where $\mathbf{f}_n^C$ is a function equal to $\mathbf{f}_n$ inside the discretization cell (e.g. a triangle) and continuous across the cell boundaries, and χ is a pulse function equal to one inside the cell and equal to zero outside. A generic element of $[Z^{\phi}]$ can be explicitly written as

$$\begin{aligned} Z_{mn}^{\phi} = {} & \frac{1}{j4\pi\omega\epsilon_0} \cdot \\ & \Bigg(\iint_{S_m} dS\, \nabla_s \cdot \mathbf{f}_m^C(\mathbf{r}) \iint_{S_n} dS' G(\mathbf{r},\mathbf{r}') \nabla'_s \cdot \mathbf{f}_n^C(\mathbf{r}') \\ & + \iint_{S_m} dS\, \nabla_s \cdot \mathbf{f}_m^C(\mathbf{r}) \oint_{\Gamma_n} d\Gamma'\, G(\mathbf{r},\mathbf{r}')\, \hat{n}_n \cdot \mathbf{f}_n^C(\mathbf{r}') \\ & - \oint_{\Gamma_m} d\Gamma\, \hat{n}_m \cdot \mathbf{f}_m^C(\mathbf{r}) \iint_{S_n} dS'\, G(\mathbf{r},\mathbf{r}') \nabla'_s \cdot \mathbf{f}_n^C(\mathbf{r}') \\ & - \oint_{\Gamma_m} d\Gamma\, \hat{n}_m \cdot \mathbf{f}_m^C(\mathbf{r}) \oint_{\Gamma_n} d\Gamma'\, G(\mathbf{r},\mathbf{r}')\, \hat{n}_n \cdot \mathbf{f}_n^C(\mathbf{r}') \Bigg) \end{aligned} \tag{5}$$

where $G(\mathbf{r},\mathbf{r}') = e^{-jk_0|\mathbf{r}-\mathbf{r}'|}/|\mathbf{r}-\mathbf{r}'|$, $k_0 = \omega\sqrt{\epsilon_0\mu_0}$, ω is the working angular frequency, ϵ_0 and μ_0 are the free space permittivity and permeability respectively. The surfaces S_m and S_n, with contours Γ_m and Γ_n, are the definition domains of the functions $\mathbf{f}_m$ and $\mathbf{f}_n$ respectively; $\hat{n}_m$ and $\hat{n}_n$ are the outer unit normals to the contours Γ_m and Γ_n respectively in the planes containing the function definition domains. If the functions $\mathbf{f}_m$ and $\mathbf{f}_n$ are div-conforming, only the first term in (5) remains. The other three terms are present when the normal component of the considered basis function does not vanish along the corresponding definition domain contour lines (non div-conforming basis functions). Along these contours, where the normal component of the basis function is different from zero, charge may accumulate; hence, as proposed in [16], [23], the so-called interior penalty concept is used to penalize the potential produced by the charges accumulated along the contours. The chosen interior penalty (IP) term is equal to

$$Z_{mn}^{\mathrm{IP}} = C \oint_{\Gamma_m} d\Gamma\, \hat{n}_m \cdot \mathbf{f}_m^C(\mathbf{r}) \oint_{\Gamma_n} d\Gamma'\, G(\mathbf{r},\mathbf{r}')\, \hat{n}_n \cdot \mathbf{f}_n^C(\mathbf{r}') \tag{6}$$

where the constant $C = 1/(j4\pi\omega\epsilon_0)$ so that Z_{mn}^{IP} exactly cancel the last term in (5) and only the first three terms in (5) need to be evaluated.

The same discretization strategy is applied to the MFIE operator, yielding

$$\begin{aligned} Z_{mn}^{\mathrm{MFIE}} = {} & \frac{1}{2} \iint_{S_m} dS\, \mathbf{f}_m(\mathbf{r}) \cdot \mathbf{f}_n(\mathbf{r}) + \\ & \iint_{S_m} dS\, \mathbf{f}_m(\mathbf{r}) \times \hat{\mathbf{n}} \cdot \iint_{S_n} dS'\, \mathbf{f}_n(\mathbf{r}') \times \nabla G(\mathbf{r},\mathbf{r}') \end{aligned} \tag{7}$$

where $\hat{\mathbf{n}}$ is the outgoing normal to the surface of the structure. For the MFIE operator there is no need to add interior penalty terms.

Alternative implementations of the discontinuous Galerkin scheme for non-conformal meshes can be also considered as recently detailed in [24], [25], and including the interior penalty stabilization term proposed in [16].

III. Residual Error Based Adaptive Refinement Scheme

In boundary element method (BEM), an infinite dimensional solution space is approximated with a finite dimensional one, therefore there is an error associated with the numerical solution. Quantifying this error is a very important aspect of numerical analysis since it can increase confidence in a solution. It can also be used to develop adaptive refinements of the BEM discretization, optimize the solution relative to the number of unknowns, and in turn reduce computational cost.

In the following subsections, an a-posteriori error indicator for estimating the relative solution error distribution is described (Sect. III-A) as well as the corresponding scheme to adaptively refine the initial mesh if the locally estimated error is above threshold (Sect. III-B).

A. Error Estimator

The proposed error estimator is residual-based, and constitutes a proper bound on an error energy measure.

To start with, we define the residual error $\mathbf{R}$ as

$$\mathbf{R}(\mathbf{r}) = \mathcal{C}\{\mathbf{J}(\mathbf{r})\} - \frac{\mathbf{E}^i_{\tan}(\mathbf{r})}{\eta} - \alpha\, \hat{\mathbf{n}} \times \mathbf{H}^i(\mathbf{r}) \tag{8}$$

where $\mathbf{E}^i_{\tan}(\mathbf{r})$ is the known incident electric field tangent to the body surface, $\mathbf{H}^i(\mathbf{r})$ is the known incident magnetic field, and the $\mathcal{C}$ is the CFIE operator

$$\mathcal{C}\{\mathbf{J}(\mathbf{r})\} = -\frac{\mathbf{E}^s_{\tan}\{\mathbf{J}(\mathbf{r})\}}{\eta} - \alpha\, \hat{\mathbf{n}} \times \mathbf{H}^s\{\mathbf{J}(\mathbf{r})\} \tag{9}$$

with $\mathbf{E}^s_{\tan}$ equal to the scattered electric field tangent to the body surface, and $\mathbf{H}^s$ equal to the scattered magnetic field.

Note that the residual error $\mathbf{R}$ is orthogonal to the space where we are seeking the solution due to the Galerkin orthogonality property. Moreover, due to the Calderon identity, the error in the approximate solution can be bounded above and below by the residual error $\mathbf{R}$ of the discretized surface integral equation. Therefore, the norm of the residual error can be used to estimate the error in the approximate solution.

Hence, we are interested in a projection of this residual error $\mathbf{R}$ into a space that can give us information on the expected advantages of a refinement, and in particular, of an h-refinement. In this sense, we recall that the Galerkin

scheme ensures zero weighed residuals when the field residual is projected onto the set of employed basis functions, so obviously we need to look at the weighted residual in a refined space; this can be achieved by the spaces spanned by functions obtained with h-refinements, e.g. half-RWG basis functions defined on mesh cells refined with respect the initial ones. The half-RWG basis functions, also called monopolar-RWG basis functions in [11] and square-integrable (L^2) basis functions in [16], are cell-based basis functions, defined as the well-known RWG basis functions, but taking into account only one of the two triangles of the RWG definition domain; as result, each triangle is support for three half-RWG basis functions.

In order to define the refined basis functions used to weight the residual error $\mathbf{R}$, all the triangular cells of the initial mesh are subdivided, through a dyadic scheme, into sub-cells, as shown in Fig. 1 for a generic k-th cell of the initial mesh. The number of levels ℓ of the dyadic subdivision scheme is related to the required accuracy of the final solution (in Fig. 1 $\ell = 2$). Then, three half-RWG basis functions are defined inside each

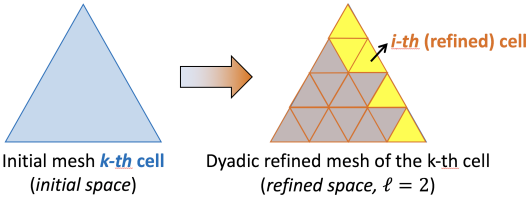

Fig. 1. Example of dyadic subdivision; left: initial space; right: refined space; highlighted in yellow the refined mesh cells above the error threshold.

i-th refined cell within the considered k-th cell.

For each cell of the refined mesh, the residual error $\mathbf{R}$ is projected on the corresponding half-RWG basis functions and normalized with respect to the basis function norm. The maximum of this normalized projection is the estimated norm of the residual error $\mathbf{R}$ and corresponds to the considered local indicator of the initial solution error (and thus of the expected advantage of a local refinement). The sought-for error estimator on the i-th refined cell within the k-th initial cell is therefore

$$\left|\left|\mathbf{R}_{k,i}^{(\ell)}\right|\right| \cong \max_{\mathbf{f}_{j(k,i)}^{(\ell)}} \frac{\left\langle \mathbf{f}_{j(k,i)}^{(\ell)}, \mathbf{R} \right\rangle}{\sqrt{\left\langle \mathbf{f}_{j(k,i)}^{(\ell)}, \mathbf{f}_{j(k,i)}^{(\ell)} \right\rangle}} \tag{10}$$

where $\mathbf{f}_{j(k,i)}^{(\ell)}$ with $j(k,i) = 1,2,3$ are the three half-RWG basis functions defined inside the considered domain.

To evaluate the error estimator in (10), we need to compute the inner product $\langle \mathbf{f}_m^{(\ell)}, \mathbf{R} \rangle$, where, to simplify the notation, the local index $j(k,i)$ has been substituted with the global index m. Substituting $\mathbf{R}$ with its expression in (8), this inner product becomes

$$\left\langle \mathbf{f}_m^{(\ell)}, \mathbf{R} \right\rangle = \left\langle \mathbf{f}_m^{(\ell)}, \mathcal{C}\left\{\mathbf{J}(\mathbf{r})\right\} - \frac{\mathbf{E}_{\tan}^{i}(\mathbf{r})}{\eta} - \alpha\, \hat{\mathbf{n}} \times \mathbf{H}^{i}(\mathbf{r}) \right\rangle, \tag{11}$$

that can be written as

$$\left\langle \mathbf{f}_m^{(\ell)}, \mathbf{R} \right\rangle = \left\langle \mathbf{f}_m^{(\ell)}, \mathcal{C}\left\{\mathbf{J}(\mathbf{r})\right\} \right\rangle - \left\langle \mathbf{f}_m^{(\ell)}, \frac{\mathbf{E}_{\tan}^{i}(\mathbf{r})}{\eta} + \alpha\, \hat{\mathbf{n}} \times \mathbf{H}^{i}(\mathbf{r}) \right\rangle. \tag{12}$$

Then, substituting $\mathbf{J}(\mathbf{r})$ with its expression in (2), equation (12) can be written in matrix format as

$$\left\langle \mathbf{f}_m^{(\ell)}, \mathbf{R} \right\rangle = \left[A_m^{(\ell)}\right] \left[I^{(\ell)}\right] - B_m^{(\ell)} \tag{13}$$

where

$$\left[A_m^{(\ell)}\right] = \frac{[Z_{\mathrm{EFIE},m}^{(\ell)}]}{\eta} + \alpha [Z_{\mathrm{MFIE},m}^{(\ell)}] \tag{14}$$

is the m-th row of the "usual" CFIE MoM matrix in the refined mesh, and

$$B_m^{(\ell)} = \frac{V_{\mathrm{EFIE},m}^{(\ell)}}{\eta} + \alpha\, V_{\mathrm{MFIE},m}^{(\ell)} \tag{15}$$

is the m-th element of the CFIE RHS vector in the refined mesh. The vector $\left[I^{(\ell)}\right]$ collects the initial current coefficients (2) *exactly* projected in the refined mesh, observing that a generic RWG (or half-RWG) basis function can be written as linear combination of the RWG (or half-RWG) basis functions defined in the same definition domain, refined via a dyadic scheme, as detailed in [26, Appendix I.A].

We note that, in any terms of (14), the test and basis functions are half-RWG functions defined on the refined mesh. Hence, the single matrix-vector product, to be performed in (13) in order to evaluate the error estimator, can be accelerated via a fast-MoM algorithm, such as the multi level fast multipole algorithm (MLFMA), including the interior penalty conditions (6) [16], [23].

Moreover, it is important to notice that the error estimator in (10) is associated to each of the *refined* mesh cells (see Fig. 1); hence, on the initial mesh cells, we obtain such as a map of the estimated error: this error map is the key ingredient to the adaptive h-refinement scheme described in the following subsection.

B. Adaptive h-refinement

In order to perform the adaptive h-refinement, the obtained error estimator values, in each cell of the refined mesh (Sect. III-A), are compared to a chosen error threshold τ: if the error estimator value is above τ, the corresponding refined cell is identified in the mesh. As an example, in Fig. 1, the refined cells, where error estimator value is above threshold, are highlighted in yellow.

The next step of the adaptive h-refinement scheme is to check which cells of the initial mesh contain at least one refined cell with the corresponding error estimator above threshold. If at least one refined cell is above τ, the corresponding initial mesh cell is divided in four sub-cells through a dyadic subdivision. If, instead, the initial mesh cell does not contain any refined mesh cell above τ, the initial mesh cell remains unchanged. Then, the same procedure is repeated recursively to all the the sub-cells in which the initial mesh cells have been divided into. The adaptive h-refinement scheme stops when the obtained sub-cells correspond to the refined mesh cells used for the error estimator evaluation (Sect. III-A). The described

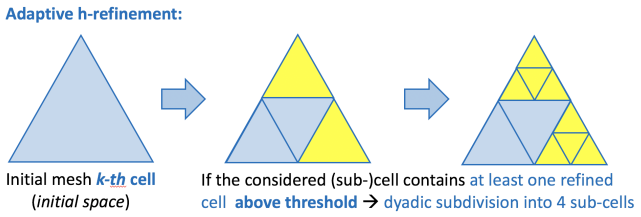

Fig. 2. Example of application of the proposed adaptive h-refinement scheme: the considered k-th cell of the initial mesh is divided into sub-cells according to the error map reported in Fig. 1; the final adaptive h-refined mesh is shown on the right.

procedure is shown with an example in Fig. 2, where the final adaptive h-refined mesh is reported on the right according to the error estimation shown in Fig. 1.

The proposed adaptive h-refinement scheme leads to a *non-conformal* mesh, as shown in Fig. 2; hence, the refined solution of the initial BEM problem can be evaluated with a fast factorization algorithm, applied to the adaptive h-refined mesh, in which a Discontinuous Galerkin scheme is implemented [16], [23].

Moreover, we notice that the choice of the error threshold τ should be related to the number of levels ℓ in which the initial mesh is subdivided into refined mesh cells to evaluate the error estimator $||\mathbf{R}_{k,i}^{(\ell)}||$, because, as stated above, the adaptive h-refinement scheme stops when the obtained mesh cells are the same as the corresponding refined mesh cells used in $||\mathbf{R}_{k,i}^{(\ell)}||$.

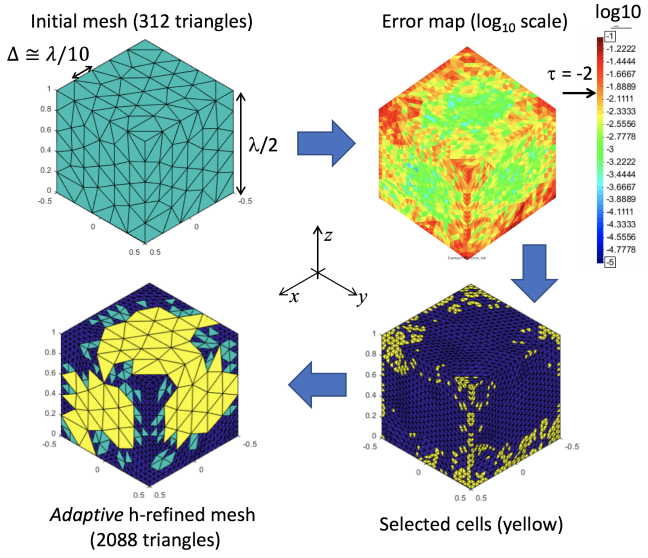

Fig. 3. Graphical description of the proposed residual error based adaptive refinement scheme.

To summarize, the whole algorithm flow can be described as follows:

1) evaluation of the unknown surface current density discretized with the initial mesh;
2) definition of the level-ℓ h-refined mesh through dyadic subdivisions of the initial mesh cells (see Fig. 1);
3) evaluation of the error estimator values on each cell of the level-ℓ h-refined mesh (10);
4) selection of the level-ℓ h-refined mesh cells whose error estimator value is above the chosen error threshold τ (see Fig. 1);
5) definition of the *adaptive* h-refined mesh according to the selected level-ℓ h-refined mesh cells (see Fig. 2);
6) evaluation of the unknown surface current density discretized with the obtained *adaptive* h-refined mesh.

The whole process is graphically described in Fig. 3 where a simple cubic structure is considered with $\log_{10}(\tau) = -2$ and $\ell = 2$.

IV. Numerical Results

A. Cubic Structure

The first considered test case is a cubic structure with side equal to $\lambda/2$, and discretized with 312 triangles, where the average mesh size is equal to $\lambda/10$ (λ is the working wavelength). The excitation is a plane wave from $(\vartheta, \varphi) = (30, 30)$ deg. with $\mathbf{E}^i = \hat{\vartheta} + \hat{\varphi}$.

The first row of Fig. 4 shows the initial mesh of the considered cube and different adaptive h-refined meshes obtained decreasing the error threshold τ (from left to right), keeping $\ell = 2$. In the second row, the corresponding error estimator values are reported in $\log_{10}$ scale: the first error map (on the left) is obtained from the initial surface current density and is used to generate all the analyzed adaptive h-refined meshes (see Sect. III-B), while the other ones are reported as a check of the quality of the surface current densities obtained with adaptive h-refined meshes. Finally, the last row shows the initial surface current density (first picture on the left) and the adaptive h-refined ones. As expected, the error estimator values decrease below the chosen error threshold τ once the corresponding adaptive h-refined mesh is applied, and the surface current densities become closer to the reference one, reported in Fig. 5. The reference surface current density has been evaluated with the level-2 h-refined conformal mesh (in the following called reference mesh), i.e. the mesh obtained through a double application of the dyadic cell subdivision scheme to all the cells of the initial mesh, and applying conventional RWG basis functions. Moreover, Fig. 6 shows the RMS error [24] of the surface current density, evaluated with the initial mesh and with the considered adaptive h-refined meshes (see with Fig. 4), with respect to the reference surface current density, defined as

$$\epsilon_{\mathrm{RMS}} = \frac{\sqrt{\int_S dS \left|\mathbf{J}\left(\mathbf{r}\right) - \mathbf{J}_{\mathrm{REF}}\left(\mathbf{r}\right)\right|^2}}{\sqrt{\int_S dS \left|\mathbf{J}_{\mathrm{REF}}\left(\mathbf{r}\right)\right|^2}} \tag{16}$$

where $\mathbf{J}_{\mathrm{REF}}$ is the reference surface current density and S the boundary of the considered PEC body. It is evident that increasing the mesh refinement according to the proposed adaptive h-refinement scheme (i.e. increasing the number of cells in Fig. 6) the ϵ_{RMS} decreases.

A further check on the obtained adaptive h-refined surface current densities is shown in Fig. 7, where the sorted error estimator values are reported in $\log_{10}$ scale for each of the considered meshes (see Fig. 4, first row). Each line of Fig. 7 corresponds to an adaptive h-refined mesh and is compared

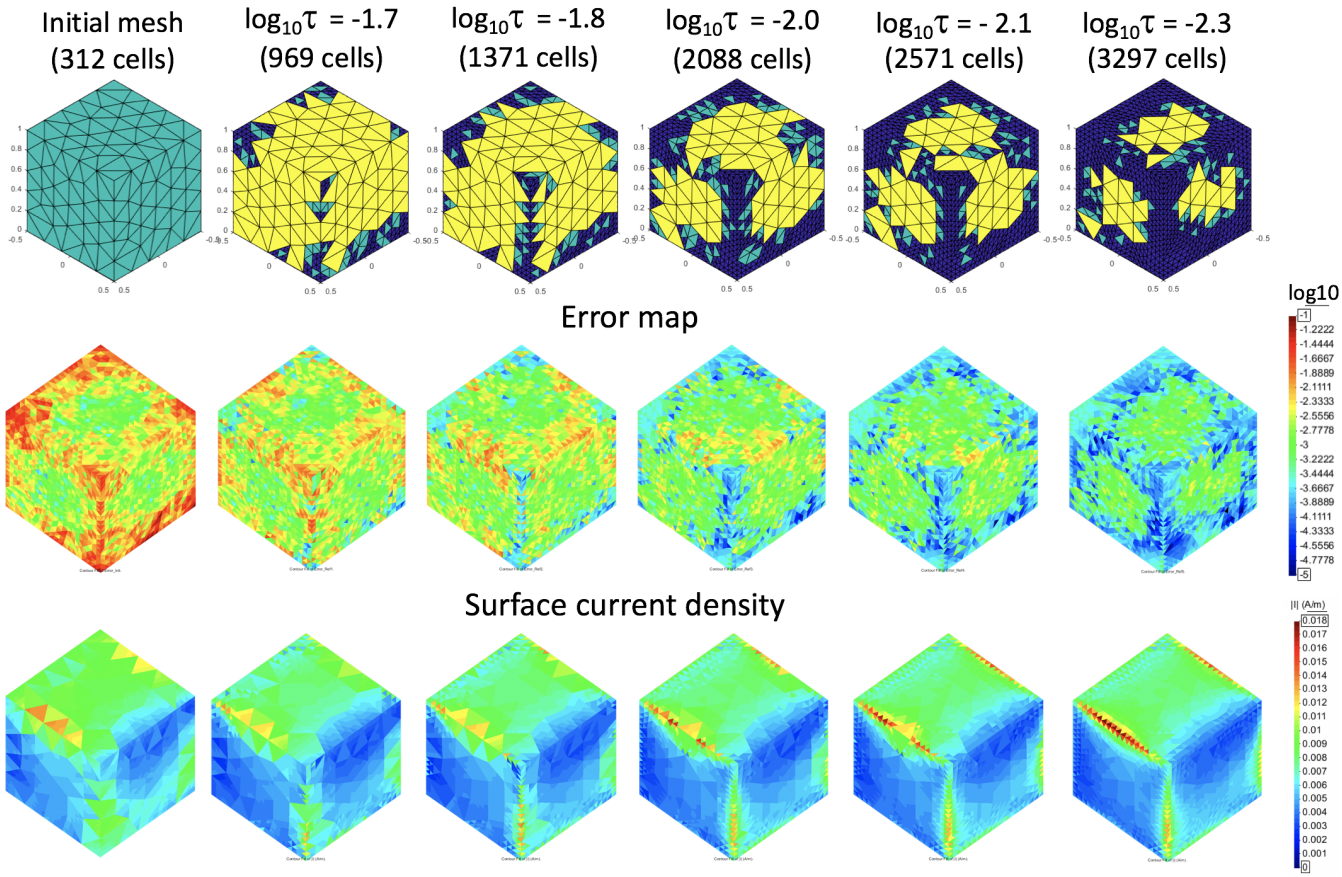

Fig. 4. Cubic structure; first row: initial mesh and adaptive h-refined meshes for different error threshold τ; second row: corresponding error map ($\log_{10}$ scale); third row: corresponding surface current density.

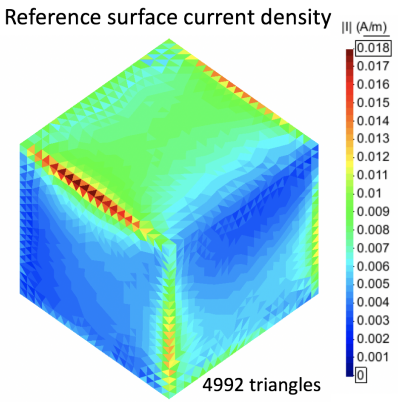

Fig. 5. Cubic structure: reference surface current density evaluated with the level-2 h-refined conformal mesh

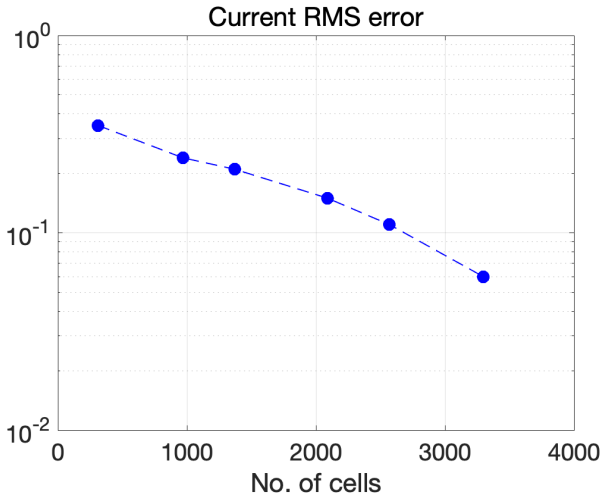

Fig. 6. Cubic structure: RMS error of the surface current density evaluated with the initial mesh and with the adaptive h-refined meshes with respect to the reference surface current density.

with the chosen error threshold τ: it is evident that the solution obtained on the adaptive h-refined mesh has error estimator values below the corresponding τ. Note that, for all cases, the number of triangles is the one of the level-2 h-refined conformal mesh (reference mesh), because the evaluation of the error estimator is associated to each cell of this mesh regardless of the considered adaptive h-refined mesh (10).

Figure 8 shows the difference of the radiated near field, in a plane parallel to one cube face at the distance of $\lambda/10$, in the case of the initial mesh and for different error threshold τ with respect to the reference near field radiated by the reference surface current density in Fig. 5. We can notice that the near

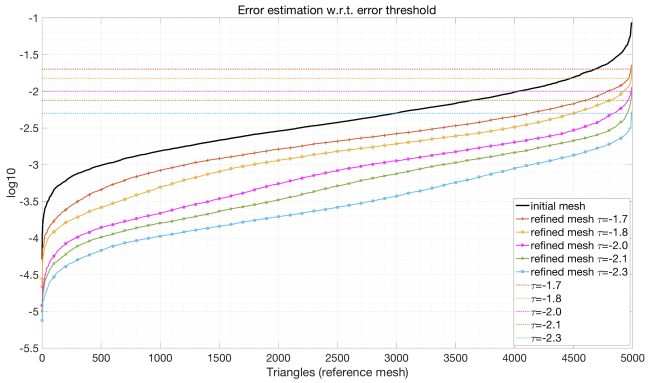

Fig. 7. Cubic structure: sorted error estimator values in $\log_{10}$ scale associated to each cell of the considered mesh; solid black line: error estimator values associated to the initial mesh; other lines: error estimator values associated to the corresponding adaptive h-refined mesh for different error threshold τ.

field difference clearly decreases once the adaptive h-refined meshes are applied, as expected observing that the proposed error estimator (10) is a residual-based.

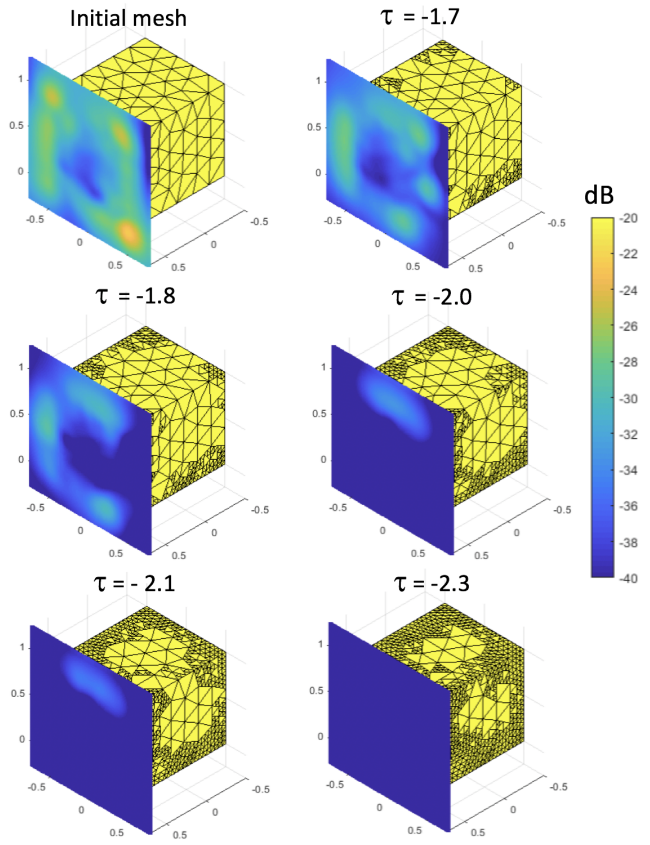

Fig. 8. Cubic structure: difference of the radiated near field in the case of the initial mesh and for different error threshold τ with respect to the reference near field radiated by the reference surface current density in Fig. 5; the plane where the near fields are evaluated is at $\lambda/10$ from the cube face.

Finally, in Fig. 9, the far field radiated by the cube is analyzed in the three main planes, i.e. xy, xz and yz planes, where the cube is oriented according to the Cartesian reference system as shown in Fig. 3. Using the adaptive h-refined meshes the radiated field is almost superimposed to the reference one, radiated by the reference surface current density in Fig. 5.

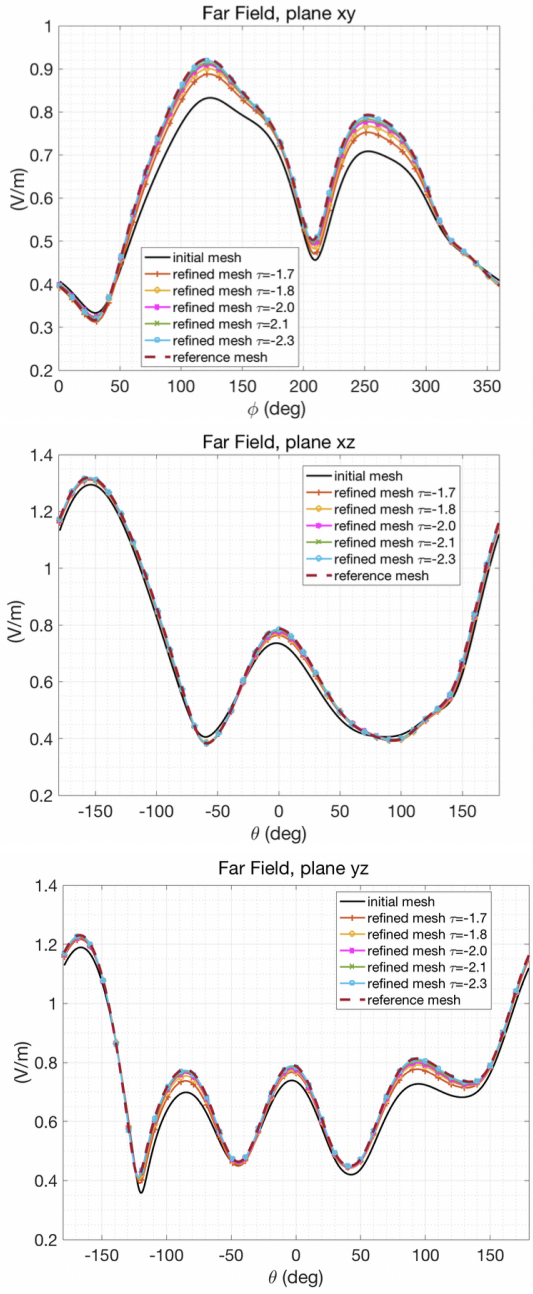

Fig. 9. Cubic structure: radiated far field in the three main planes comparing the case of the initial mesh, adaptive h-refined meshes for different error threshold τ and the reference mesh.

B. *Realistic multi-scale structure*

The next analyzed structure is the morphed version of a "Rafale" aircraft with maximum length equal to $\sim 7\lambda$ and excited by a plane wave from $(\vartheta, \varphi) = (30, 30)$ deg. with $\mathbf{E}^i = \hat{\vartheta} + \hat{\varphi}$.

The initial mesh, shown in Fig. 10.a, is formed by 5.324 triangles with minimum and maximum size equal to $\sim \lambda/150$ and $\sim \lambda/5$ respectively. The initial surface current density (see Fig. 11.a) is given in input to the error estimator (10)

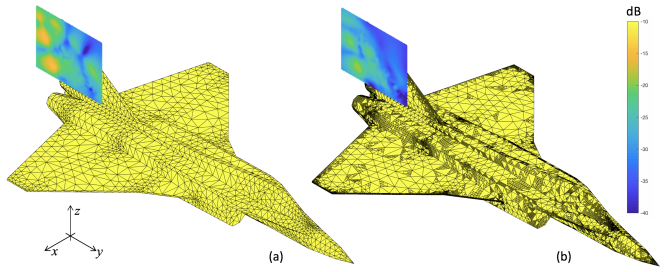

Fig. 10. Rafale aircraft; (a): initial mesh; (b): adaptive h-refined mesh; difference of the radiated near field with respect to the reference one (dB)

with $\ell = 2$, obtaining the error map shown in Fig. 12.a. The error map is compared to the error threshold $\log_{10}(\tau) = -2.1$, highlighting that the 18% of the level-2 triangles are above threshold.

Then, the adaptive h-refined mesh is generated accordingly, as shown in Fig. 10.b; the total number of triangle is equal to 28.952, with the same maximum triangle size as the initial mesh, and minimum triangle size reduced to $\sim \lambda/600$. As a first check, the error map is evaluated also for the obtained adaptive h-refined mesh, where now the level-2 triangles above threshold are reduce to less than 4% (see Fig. 12.b). The adaptive h-refined surface density current is shown in Fig. 11.b.

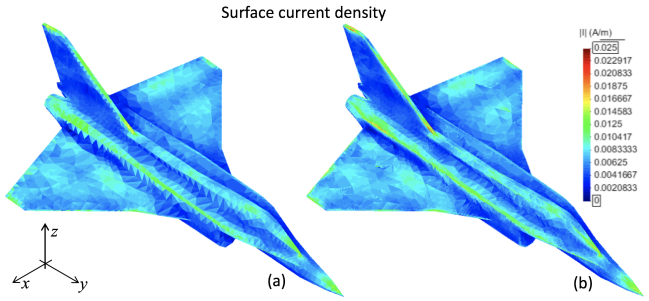

Fig. 11. Rafale aircraft surface current density; (a): initial mesh; (b): adaptive h-refined mesh.

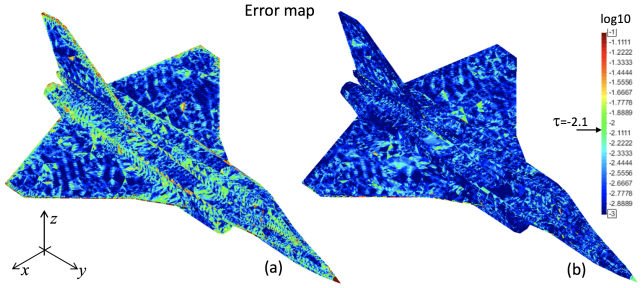

Fig. 12. Rafale aircraft error map; (a): initial mesh; (b): adaptive mesh.

To better compare the initial and h-refined surface density currents to the reference one, obtained with a level-2 h-refined conformal mesh formed by 85.184 triangles (see Fig. 13), some details of the aircraft are highlighted in Fig. 14, where the first column corresponds to the initial mesh solution, the second one to the adaptive h-refined solution and the last one

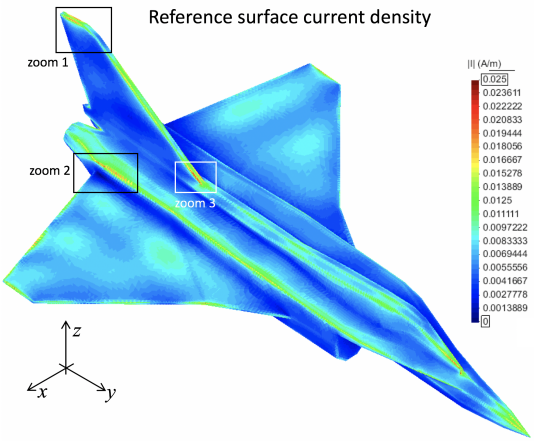

Fig. 13. Rafale aircraft: reference surface current density obtained with the level-2 h-refined conformal mesh (reference mesh).

to the reference solution. It is evident that the adaptive h-refined mesh allows to significant improve the accuracy of the surface density current, in particular close to geometrical asperities such as edges and corners, keeping the total number mesh triangles around $1/3$ with respect to the reference mesh.

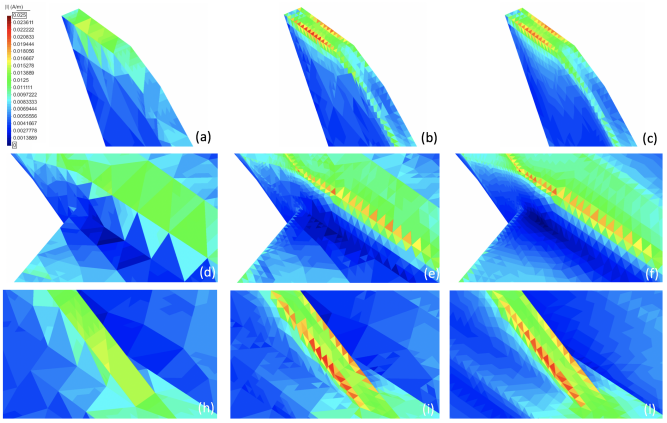

Fig. 14. Rafale aircraft: details of the surface current densities; (a)-(c): zoom 1 in Fig. 13; (d)-(f): zoom 2 in Fig. 13; (h)-(l): zoom 3 in Fig. 13; the 1st column is obtained with the initial mesh, the 2nd with the adaptive h-refined mesh, and the 3rd with the reference mesh.

Finally, Fig. 10 shows the difference of the radiated near field with respect to the reference one in the case of the initial mesh (a), and in the case of the adaptive h-refined mesh (b), at $\lambda/10$ from the aircraft tail; the field error is strongly reduced once the adaptive h-refined mesh is applied.

V. Conclusion and Perspectives

In this paper, we presented an adaptive and automatic h-refinement scheme for the analysis of multi-scale structures, able to enrich the approximations locally, at element level, for a prescribed threshold. A local measure of the boundary condition error is obtained via testing on local refined half-RWG basis functions. The adaptive h-refined mesh is effected via non-conformal sub-meshing and Discontinuous-Galerkin.

The next steps of the research activity are the development of guidelines for the error threshold choice with respect to the desired solution accuracy, and the investigation of an adaptive h-refined meshing that avoids the need of the Discontinuous-Galerkin solution scheme.

REFERENCES

[1] M. M. Botha and D. B. Davidson, "The implicit, element residual method for a posteriori error estimation in fe-bi analysis," *IEEE Transactions on Antennas and Propagation*, vol. 54, no. 1, pp. 255–258, Jan. 2006.

[2] M. M. Botha and D. B. Davidson, "An explicit a posteriori error indicator for electromagnetic, finite element-boundary integral analysis," *IEEE Transactions on Antennas and Propagation*, vol. 53, no. 11, pp. 3717–3725, Nov. 2005.

[3] D. Xue, L. Demkowicz, and L. Hao, "A 3-d *hp* finite/infinite element method to calculate power deposition in the human head," *IEEE Transactions on Biomedical Engineering*, vol. 54, no. 4, pp. 734–741, April 2007.

[4] P. Paul and J. P. Webb, "Finite element analysis of electromagnetic scattering using *p* -adaption and an iterative absorbing boundary condition," *IEEE Transactions on Magnetics*, vol. 46, no. 8, pp. 3361–3364, Aug. 2010.

[5] N. Heuer, "An hp-adaptive refinement strategy for hypersingular operators on surfaces," *Numerical Methods for Partial Differential Equations*, vol. 18, no. 3, pp. 396–419, 2002. [Online]. Available: http://dx.doi.org/10.1002/num.10011

[6] C. Erath, S. Funken, P. Goldenits, and D. Praetorius, "Simple error estimators for the galerkin BEM for some hypersingular integral equation in 2D," *Applicable Analysis*, vol. 92, no. 6, pp. 1194–1216, 2013. [Online]. Available: http://dx.doi.org/10.1080/00036811.2012.661045

[7] C. Dominguez and N. Heuer, "A posteriori error analysis for a boundary element method with nonconforming domain decomposition," *Numerical Methods for Partial Differential Equations*, vol. 30, no. 3, pp. 947–963, 2014. [Online]. Available: http://dx.doi.org/10.1002/num.21847

[8] M. Aurada, M. Feischl, T. Fhrer, M. Karkulik, and D. Praetorius, "Energy norm based error estimators for adaptive BEM for hypersingular integral equations," *Applied Numerical Mathematics*, vol. 95, pp. 15 – 35, 2015, fourth Chilean Workshop on Numerical Analysis of Partial Differential Equations (WONAPDE 2013). [Online]. Available: http://www.sciencedirect.com/science/article/pii/S0168927414000178

[9] U. Saeed and A. F. Peterson, "Explicit local error estimators for electromagnetic integral equations," *IEEE Transactions on Antennas and Propagation*, vol. 63, no. 3, pp. 1159–1163, Mar. 2015.

[10] F. G. Bogdanov, R. G. Jobava, and S. Frei, "Estimating accuracy of MoM solutions on arbitrary triangulated 3-D geometries based on examination of boundary conditions performance and accurate derivation of scattered fields," *J. Elecromagn. Waves and Appl.*, vol. 18, no. 7, pp. 879–897, May 2004.

[11] E. Ubeda and J. M. Rius, "Novel monopolar MoM-MFIE discretization for the scattering analysis of small objects," *IEEE Transactions on Antennas and Propagation*, vol. 54, no. 1, pp. 50–57, Jan. 2006.

[12] E. Ubeda, J. M. Rius, and A. Heldring, "Nonconforming discretization of the electric-field integral equation for closed perfectly conducting objects," *IEEE Transactions on Antennas and Propagation*, vol. 62, no. 8, pp. 4171–4186, Aug. 2014.

[13] E. Ubeda, J. M. Rius, A. Heldring, and I. Sekulic, "Volumetric testing parallel to the boundary surface for a nonconforming discretization of the electric-field integral equation," *IEEE Transactions on Antennas and Propagation*, vol. 63, no. 7, pp. 3286–3291, July 2015.

[14] S. K. Kim and A. F. Peterson, "Adaptive h-refinement for the rwg-based efie," *IEEE Journal on multiscale and multiphysics computational techniques*, vol. 3, pp. 58–65, 2018.

[15] G. C. Hsiao and R. E. Kleinman, "Mathematical foundations for error estimation in numerical solutions of integral equations in electromagnetics," *IEEE Transactions on Antennas and Propagation*, vol. 45, no. 3, pp. 316–328, Mar. 1997.

[16] Z. Peng, K.-H. Lim, and J.-F. Lee, "A discontinuous galerkin surface integral equation method for electromagnetic wave scattering from non-penetrable targets," *IEEE Transactions on Antennas and Propagation*, vol. 61, no. 7, pp. 3617–3628, July 2013.

[17] Z. Peng, R. Hiptmair, Y. Shao, and B. MacKie-Mason, "Domain decomposition preconditioning for surface integral equations in solving challenging electromagnetic scattering problems," *IEEE Transactions on Antennas and Propagation*, vol. 64, no. 1, pp. 210–223, Jan. 2016.

[18] J. A. Tobon Vasquez, Z. Peng, J.-F. Lee, G. Vecchi, and F. Vipiana, "Automatic error estimator and mesh refinement for the CFIE," presented at the 2018 IEEE International Symposium on Antennas and Propagation and USNC/URSI National Radio Science Meeting, Boston, MA, USA, July 8–13 2018.

[19] J. A. Tobon Vasquez, F. Vipiana, G. Vecchi, Z. Peng, and J.-F. Lee, "Multi-scale structures analysis using automatic h-refinement and discontinuous galerkin integral equation," presented at the 2013 IEEE International Symposium on Antennas and Propagation and USNC/URSI National Radio Science Meeting, Orlando, FL, USA, July 2013, pp. 446–447.

[20] J. A. Tobon Vasquez, F. Vipiana, Z. Peng, J.-F. Lee, and G. Vecchi, "An automatic h-refinement scheme for discontinuous galerkin integral equations in the analysis of multi-scale structures," presented at the 2013 7th European Conference on Antennas and Propagation (EuCAP), Gothenburg, Sweden, April 2013, pp. 4048–4049.

[21] J. A. Tobon Vasquez, A. Francavilla, F. Vipiana, G. Vecchi, Z. Peng, and J.-F. Lee, "Automatic h-refinement through a-posteriori error estimation and discontinous galerkin," presented at the 2015 IEEE International Conference on Computational Electromagnetics (ICCEM), Hong Kong, Feb. 2015, pp. 333–334.

[22] S. Rao, D. Wilton, and A. Glisson, "Electromagnetic scattering by surfaces of arbitrary shape," *IEEE Transactions on Antennas and Propagation*, vol. 30, no. 3, pp. 409–418, May 1982.

[23] M. A. Echeverri Bautista, F. Vipiana, M. A. Francavilla, J. A. Tobon Vasquez, and G. Vecchi, "A non-conformal domain decomposition scheme for the analysis of multi-scale structures," *IEEE Transactions on Antennas and Propagation*, vol. 63, no. 8, pp. 3548–3560, Aug. 2015.

[24] Y. Chen, X. Tian, S.-X. Peng, K.-H. Lim, and J.-F. Lee, "A reverse operation self-consistent evaluation approach for singular integrals in the SIE analysis of PEC targets," *IEEE Transactions on Antennas and Propagation*, vol. 66, no. 4, pp. 1914–1924, April 2018.

[25] Y. Chen, D. Li, J. Hu, and J.-F. Lee, "A nonconformal surface integral equation for electromagnetic scattering by multiscale conducting objects," *IEEE J. Multiscale Multiphys. Comput. Tech.*, vol. 3, pp. 225–234, 2018.

[26] F. Vipiana, P. Pirinoli, and G. Vecchi, "A multiresolution method of moments for triangular meshes," *IEEE Transactions on Antennas and Propagation*, vol. 53, no. 7, pp. 2247–2258, July 2005.